ADVANCED FUNCTIONAL MATERIALS
www.afm-journal.de

Enabling Conversion-Type Iron Fluoride Cathode by Halide-Based Solid Electrolyte

Bowen Shao, Sha Tan, Yonglin Huang, Lifu Zhang, Jian Shi, Xiao-Qing Yang, Enyuan Hu, and Fudong Han**

The practical application of low-cost and energy-dense iron fluoride cathodes is hindered by the first cycle electrochemical irreversibility, cycling instability, and large voltage hysteresis. Here, it is reported that these challenges may be overcome by the utilization of halide-based solid electrolytes (SEs). The excellent electrochemical stability of halide-based SEs enables a complete conversion and deconversion of FeF_2 that cannot be achieved with sulfide-based SEs. Due to restricted and reversible decomposition of SE, prevention of Fe dissolution, mechanical confinement of active material, as well as improved electrode kinetics, solid-state FeF_2 cathode with halide-based SE demonstrates superior electrochemical performance compared with FeF_2 electrodes in liquid electrolytes, with a high 1st cycle coulombic efficiency (≈100%), high specific capacity (≈600 mAh g^{-1}), long cycle life (>100 cycles), and high-rate performance (up to 2 C). The results suggest solidifying the batteries is a viable approach to addressing the long-standing key challenges of iron fluoride cathodes.

1. Introduction

There is an intense interest in revitalizing the conversion-type cathode for lithium-ion batteries because (i) it offers the potential to provide the highest energy density for powering next-generation electric vehicles and all-electric passenger aircraft,[1–5] and (ii) it eliminates the utilization of scarce, expensive, and toxic transition metals such as cobalt and nickel that are indispensable elements in the state-of-the-art layered-oxide cathode materials.[6–14] Among the conversion-type cathodes, iron fluorides, namely FeF_2 or FeF_3, which are made from extremely low-cost materials (e.g., iron: ≈0.1 US\$ kg^{-1}), are representative examples that yield very high specific capacities at attractive voltages.[15–24] It should be noted that while sulfur as a conversion-type cathode has already been used in the batteries for unmanned air vehicles,[25] FeF_2 offers a higher volumetric capacity (2002 mA h cm^{-3}) than sulfur (1935 mA h cm^{-3}) at a slightly higher theoretical potential and both fluorine and iron are more abundant in the Earth's crust than sulfur.[8]

Despite the great promise of storing two to three times more energy per given unit mass than the conventional cathodes, the practical application of iron fluoride cathodes has been hindered by multiple challenges. Due to the irreversible electrolyte decomposition and incomplete re-conversion,[26] a low coulombic efficiency (<80%) can be observed for the first cycle.[2,27] The cycling instability of iron fluoride cathodes is also observed due to mechanical failure (e.g., displacement of active particles, particle decohesion, and pulverization) and chemical degradations (dissolution of transition metal in the electrolyte, and continuous formation of solid electrolyte interphase).[4,7,8,27] Previous studies commonly demonstrate only a few cycles (20–50) or exhibit apparent capacity decay within 100 cycles.[7,27] The capacity decay seems to be worse at elevated temperatures due to the enhanced degradations.[7] Moreover, a large voltage hysteresis (from several hundred mV to 2 V) can usually be observed for iron fluoride cathodes during charge and discharge, leading to a low round-trip efficiency.[4,5,24,28,29] All these obstacles should be overcome if this class of materials is ever to become viable for practical applications.

Here we propose that the intrinsic limitations of iron fluoride cathodes may be addressed by using solid electrolytes (SEs) (**Figure 1**). Even though the thermodynamic electrochemical stability of many SEs is limited,[30–32] due to restricted contact between SE and active material/carbon additives, the decomposition of SE is expected to be less severe than that in the liquid-electrolyte based batteries.[10,33,34] Due to the non-flowable and non-infiltrative feature of SE, the formation of solid electrolyte interphase (SEI) in solid-state batteries is also expected to be less dynamic (i.e., are frozen at the solid-solid interface)[33] than that in the liquid electrolytes and therefore the utilization of SE can effectively improve the coulombic efficiencies during charge/discharge cycles by minimizing the need to

B. Shao, Y. Huang, F. Han
Department of Mechanical, Aerospace and Nuclear Engineering
Rensselaer Polytechnic Institute
Troy, NY 12180, USA
E-mail: hanf2@rpi.edu

S. Tan, X.-Q. Yang, E. Hu
Chemistry Division
Brookhaven National Laboratory
Upton, NY 11973, USA
E-mail: enhu@bnl.gov

L. Zhang, J. Shi
Department of Materials Science and Engineering
Rensselaer Polytechnic Institute
Troy, NY 12180, USA

The ORCID identification number(s) for the author(s) of this article can be found under https://doi.org/10.1002/adfm.202206845.

DOI: 10.1002/adfm.202206845

 © 2022 Wiley-VCH GmbH

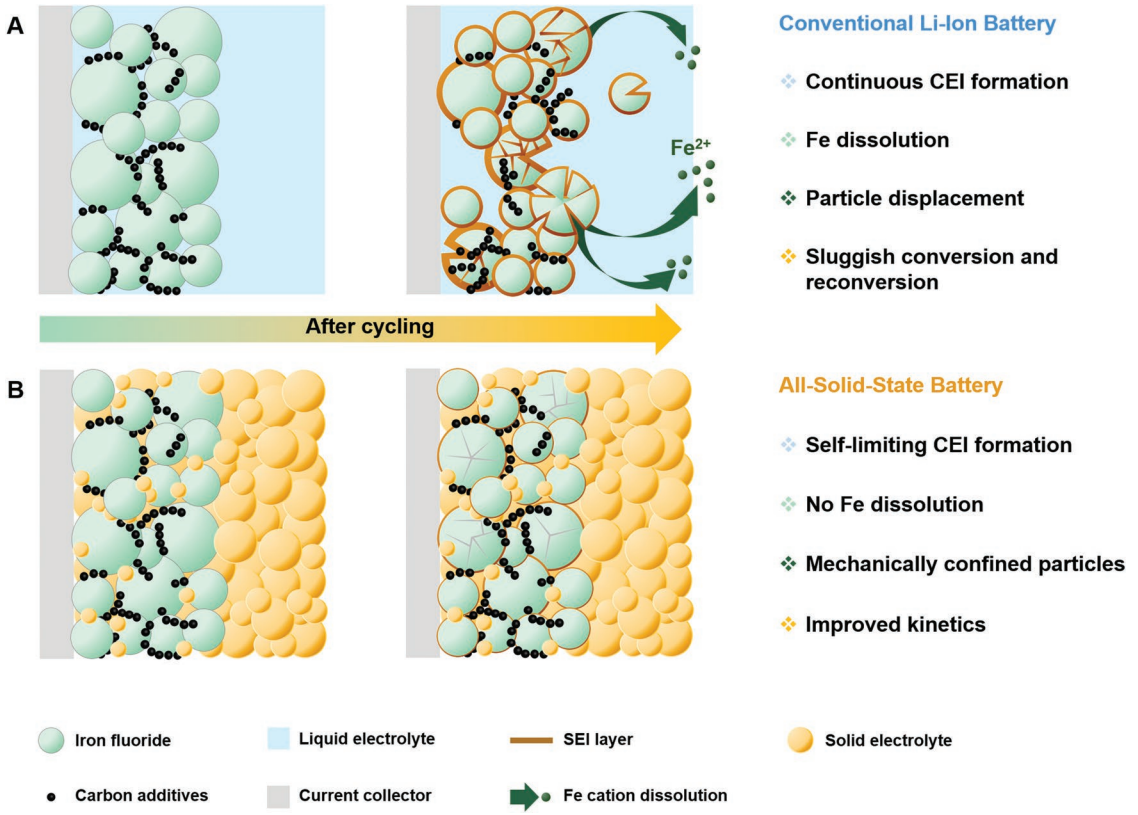

Figure 1. Overcoming key challenges of conversion-type cathodes by solid electrolytes. A) The key challenges in the conventional conversion-type cathodes in liquid-electrolyte-based batteries: cathode active material dissolution, cathode particle displacement, continuous CEI formation, and sluggish conversion and reconversion. B) The utilization of solid electrolytes prevents transition metal ion dissolution, enables self-limiting CEI formation, provides a mechanically confined environment for cathode particles, and improves electrode kinetics due to the elimination of concentration polarization and the high concentration of Li ions in the electrolyte.

continually re-form part of the SEI, especially at the surfaces of newly formed cracks or voids within the electrode. Moreover, the decomposition of many SEs (e.g., sulfide-based SEs) is reversible and therefore does not contribute to the irreversible capacity of the electrodes.[30,35] All of these are helpful in improving the electrochemical reversibility of the electrodes. Utilizing SEs with iron fluoride cathodes could also improve the cycle life based on the following reasons. First, the above-mentioned factors that can lead to increases in the coulombic efficiency during charge/discharge cycles will also help improve the cycling stability. Second, the dense electrode composite with SE and carbon as confinements helps mitigate the displacement of active material, thus improving its structural stability during long-term cycling. Furthermore, the utilization of SE eliminates the capacity loss due to the dissolution of Fe in the electrolyte.[8,27] While the voltage hysteresis of conversion-type cathodes is heavily related to the intrinsic properties of the electrode material itself, it has been reported that electrolyte optimization can be used as an effective way to reduce the voltage hysteresis.[6,8] Since it has been widely reported that the voltage hysteresis for conversion-type electrodes is kinetic rather than thermodynamic in nature,[24,28,29] the excellent attributes of SEs can help improve battery kinetics due to i) elimination of concentration polarization and solvation/de-solvation processes,[31,36] ii) higher conductivity of some SEs than liquid electrolytes,[37] and iii) higher concentration of Li ion per unit volume in the electrolyte.[36] The excellent thermal stability of SEs also enables battery operation at an elevated temperature if needed to further lower the voltage hysteresis. In addition, ternary metal fluorides ($Cu_xFe_{1-y}F_2$)[24] and Co and O co-substituted iron fluorides[5] have been demonstrated to exhibit very low-voltage hysteresis during charge/discharge cycles, the utilization of SEs could also improve their electrochemical performances by preventing dissolutions of Cu[38] and Co[39,40] in the electrolyte.

As a proof of concept of using SEs to address the key challenges of conversion-type iron fluoride cathodes, here we demonstrate the electrochemical behaviors of FeF_2 cathode in solid-state batteries. Two representative SEs, amorphous $75Li_2S$-$25P_2S_5$ (LPS) and glass-ceramic Li_3YCl_6 (LYC), for the sulfide- and halide-based conductors, respectively, are used in this study.[41–48] The electrochemical characteristics of FeF_2 in LPS SE exhibit drastic deviations from that in the liquid electrolyte batteries. Detailed characterizations by ex situ X-ray diffraction (XRD) and X-ray absorption spectroscopy (XAS) revealed that irreversible transformation from FeF_2 to FeS occurs when testing FeF_2 in the sulfide-based SE. Changing the SE to halide-based materials has been shown to enable a complete conversion and reconversion of FeF_2, with a specific capacity ≈600 mA h g^{-1} at 0.1 C at an average potential of ≈2.6 V. We

© 2022 Wiley-VCH GmbH

further demonstrate amorphization of the FeF_2-LYC composite as an effective approach to further improve the electrochemical performance of FeF_2 in halide-based SEs. The amorphous FeF_2-LYC cathode exhibited a superior electrochemical performance compared with FeF_2 cathodes tested in liquid electrolytes. To the best of our knowledge, this is the first report on the investigation of iron fluoride cathodes with inorganic SE.

2. Results and Discussion

2.1. Galvanostatic Profiles and Structural Evolution during Charge and Discharge

The electrochemical properties of FeF_2 were evaluated in a lab-scale solid-state cell using a composite consisting of FeF_2, LPS or LYC, and vapor-grown carbon fiber (VGCF) as the cathode, LYC, or LPS as the SE and Li–In alloy as the anode. The particle size of FeF_2 was first reduced to nanoscale by ball milling (Figure S1, Supporting Information), and the FeF_2 nanoparticles were then further ball-milled with SE and VGCF with the aim to achieve a uniform distribution of FeF_2, SE, and VGCF, although micron-sized regions that corresponds to FeF_2 and carbon can be observed in the ball-milled FeF_2-LPS and FeF_2-LYC cathode composites (Figure S2, Supporting Information). **Figure 2**A shows the charge/discharge curves of FeF_2 cathodes in LPS. Surprisingly, FeF_2 shows distinct electrochemical behavior in LPS compared with that in the liquid electrolyte.[2,49,50] Two sloping plateaus at round 2.0 and 1.5 V can be observed for the first discharge process, while the first charge profile shows only one plateau of ≈2.1 V. For the subsequent cycles, the charge–discharge curves show one sloping plateau at ≈ 2.2 V for charge and one sloping plateau at ≈1.8 V for discharge. The average potential is much lower than the theoretical potential of FeF_2 (2.6 V), implying the irreversible transformation of FeF_2 during the first discharge process. The large deviation from the electrochemical behavior of FeF_2 cathode is also supported by the fact that the delivered capacity (≈1200 mA h g^{-1} for the first discharge and ≈ 900 mA h g^{-1} for the first charge) is much higher than the theoretical value (571 mA h g^{-1}). It is likely that the SE, namely LPS, in the cathode composite largely participates in the redox reaction. The reversible decomposition of sulfide electrolytes has been reported in many previous works[30,51] and is also supported by the large capacity of the cathode consisting of VGCF and LPS (Figure S3A,C, Supporting Information). The electrochemical behavior of FeF_2 in lithium argyrodite

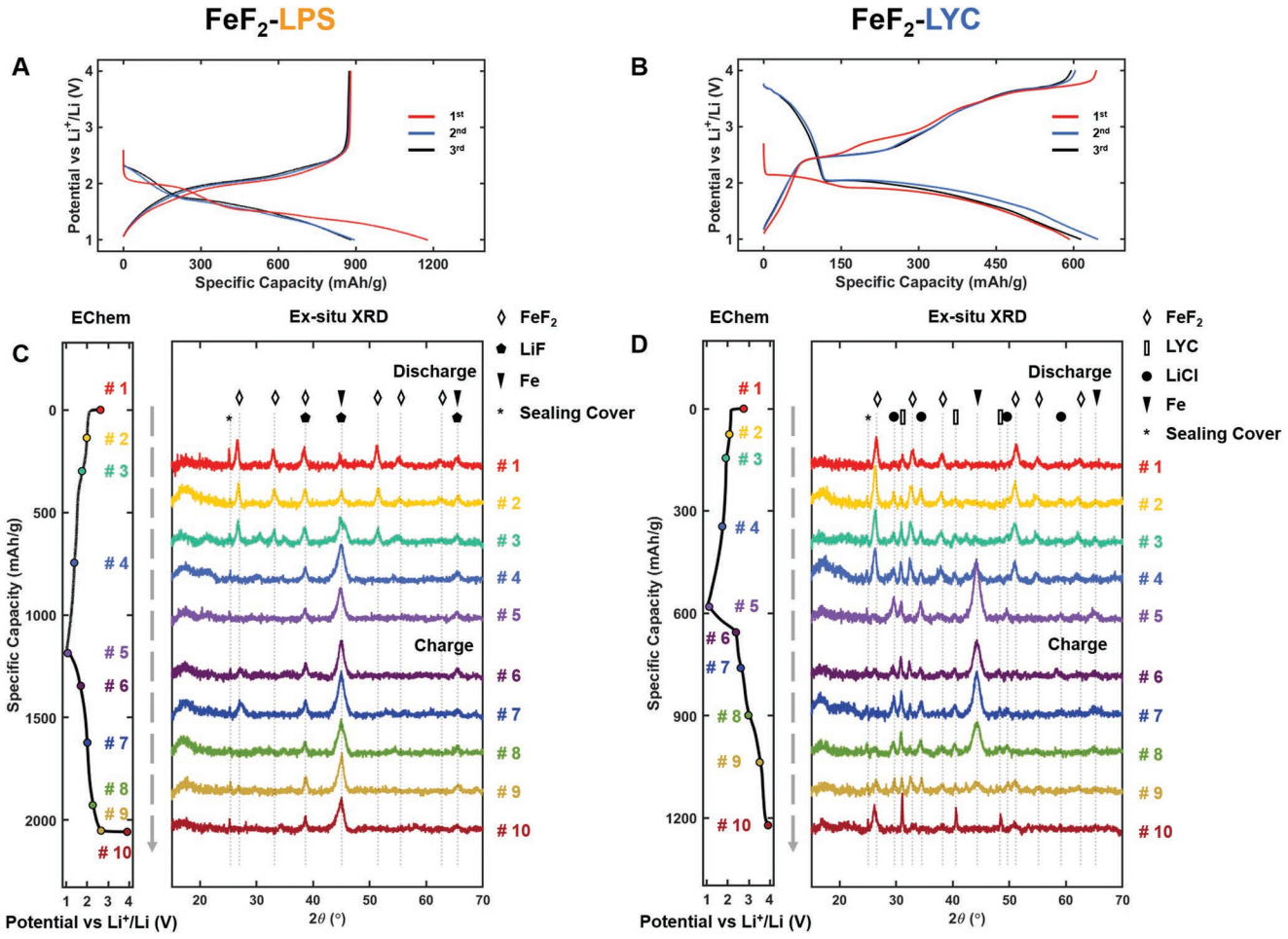

Figure 2. Galvanostatic charge/discharge profiles and structural evolution of FeF_2 cathode composite. Charge/discharge profiles of A) FeF_2-LPS and B) FeF_2-LYC for the first three cycles at 0.1 C and 60 °C. Ex situ XRD patterns of C) FeF_2-LPS and D) FeF_2-LYC.

© 2022 Wiley-VCH GmbH

Li_6PS_5Cl SE are very similar to those tested in LPS (Figure S4, Supporting Information), suggesting that the irreversible transformation of FeF_2 seems to be universal in sulfide-based SEs.

On the other hand, the electrode reactions of FeF_2 in LYC SEs occur at much higher potentials. Two sloping plateaus at 2.1 and 1.9 V can be observed for the first discharge process and the first charge process shows two plateaus at 2.4 and 3.4 V, respectively, leading to an average voltage close to the theoretical potential of FeF_2 (2.6 V).[52] The initial discharge capacity (≈600 mA h g^{-1}) is a little higher than the theoretical capacity of FeF_2, indicative of slight decomposition of LYC (Figure S3B,D, Supporting Information). The reversible decomposition of LYC also leads to a higher capacity for the first charging process (≈640 mA h g^{-1}), resulting in a high coulombic efficiency for the 1st cycle (≈106%). The higher-than-100% coulombic efficiency for the first cycle indicates that the LYC SEs can serve as a prelithiation agent that can provide additional Li for the cathode.[53,54] The coulombic efficiency reaches >97% for the second and third cycles. Compared with the electrochemical behavior of FeF_2 in liquid electrolytes,[2,49,50] the electrode reactions of FeF_2 in LYC occur at similar voltage but with a higher specific capacity and a higher coulombic efficiency.

To understand the structural evolution of FeF_2 cathode in different SEs, the XRD patterns of the cathode composites at different states of charge were collected (Figure 2C,D). The diffraction patterns of each component of the cathode composites including amorphous LPS, glass-ceramic LYC, and the nanocrystalline FeF_2, are included in the supplementary information (Figure S5, Supporting Information). While the main peaks of the diffraction pattern of as-prepared FeF_2-LPS cathode composite can be ascribed to FeF_2, the peaks at 45° and 66° are likely attributed to LiF (Figure S5A, Supporting Information). The existence of LiF indicates the chemical reactions between FeF_2 and LPS even during the ball-milling process to synthesize the cathode composite. The XRD pattern of as-prepared FeF_2-LYC cathode composite shows no other phases except for FeF_2 and LYC (Figure S5B, Supporting Information), suggesting the chemical stability between FeF_2 and LYC during synthesis.

During the first discharge of FeF_2-LPS cathode, the Bragg peaks for FeF_2 diminish and the peaks for LiF and Fe appear (Figure 2C). At the end of discharge (point 5 shown in Figure 2C), only the peaks for LiF and Fe can be observed. The peaks for LiF and Fe remain during the subsequent charging process, and more importantly, no peaks for FeF_2 can be observed during the subsequent charging process (Figure 2C). The remaining peaks for Fe and LiF and the disappearance of FeF_2 after charging indicate significant changes occur in the redox behavior of the FeF_2-LPS cathode after the first discharge. The ex situ XRD results are also consistent with the abnormal electrochemical characteristic of FeF_2-LPS shown in Figure 2A.

For the FeF_2-LYC cathode, the Bragg peaks of Fe appear with the increase of the depth of discharge (Figure 2D), suggesting the conversion of FeF_2 to Fe and LiF, even though the Bragg peaks for LiF cannot be clearly distinguished due to overlapping with the peaks of LYC and Fe. Additional peaks at 30°, 35°, and 50° appear during the initial discharge, and those peaks can be attributed to LiCl, indicating that LYC also participate in the redox reaction. During charge, the intensity of Fe peaks gradually decreases and the diffraction peaks of FeF_2 gradually increase, as can be clearly seen from its peak at 27° (Figure 2D). The formation of FeF_2 confirms successful reconversion to FeF_2 during charging. The intensity of the peaks corresponding to LiCl decrease at the end of charging process and no LiCl can be observed at the end of the first charging process.

The ex situ XRD results show distinctly different behavior of FeF_2 cathode in different SEs. With LPS SE, significant change in the reaction mechanism of FeF_2 after the first discharge. The remaining XRD peaks for Fe and LiF after charging indicates that the high specific capacity (≈900 mA h g^{-1}) during charge cannot be attributed to the reconversion process of FeF_2. On the other hand, the utilization of LYC SE can enable a complete conversion and reconversion process of FeF_2, although LYC also participated the redox reaction at the high voltages as indicated by the appearance and disappearance of LiCl.

2.2. Evolution of Fe during Charge and Discharge

To further understand the mechanism of the electrolyte-dependent conversion reaction of FeF_2, we resort to XAS to directly probe the evolution of Fe in the bulk electrodes. Fe *K*-edge XAS spectra were collected for electrodes at various states of charge during the first cycle (**Figure 3**). The change in Fe oxidization state was monitored by X-ray absorption near-edge structure (XANES) (Figure 3A,C) and the local structure was revealed by extended X-ray absorption fine structure (EXAFS) (Figure 3B,D). The relative mole fraction of different Fe species was also estimated by linear combination fitting analysis (LCA) and the fitting results are included in Figure S6 (Supporting Information). It should be noted that the accuracy of the LCA fitting highly depends on the number of fitting compounds and the features of fitting spectra, and therefore the fitting results can only be used as a rough estimate for the relative contents of the species.[55,56] The absorption edge of the XANES spectra of as-prepared FeF_2-LPS shifted to lower energies and pre-edge features corresponding to FeS can be observed, indicating the co-existence of FeF_2 and FeS in the as-prepared FeF_2-LPS cathode. The formation of FeS during electrode synthesis is also supported by the Auger mapping in the as-prepared FeF_2-LPS cathode composite where a micron-sized region that is rich in Fe and S but poor in F can be observed (Figure S7, Supporting Information). The formation of FeS further confirms the reaction between FeF_2 and LPS during the ball-milling synthesis process. Combining with the XRD results (Figure S5A, Supporting Information), it can be concluded that the reaction between FeF_2 and LPS leads to the formation of FeS and LiF. The absence of diffraction peaks of FeS is likely due to its small size or low crystallinity. The XANES and EXAFS spectra of as-prepared FeF_2-LYC shows very similar feature as the spectra of FeF_2 standard sample, indicative of the stability between FeF_2 and LYC during synthesis.

During discharge of FeF_2-LPS cathode, both FeF_2 and FeS in the FeF_2-LPS cathode convert to Fe as suggested by the rising feature at low incident energy between 7110 and 7115 eV. The conversion of FeS to Fe is also consistent with the electrochemistry data that show redox behavior deviates significantly from typical FeF_2 conversion reactions (Figure 2A). During charge, the absorption edge of XANES spectra shifted to higher

© 2022 Wiley-VCH GmbH

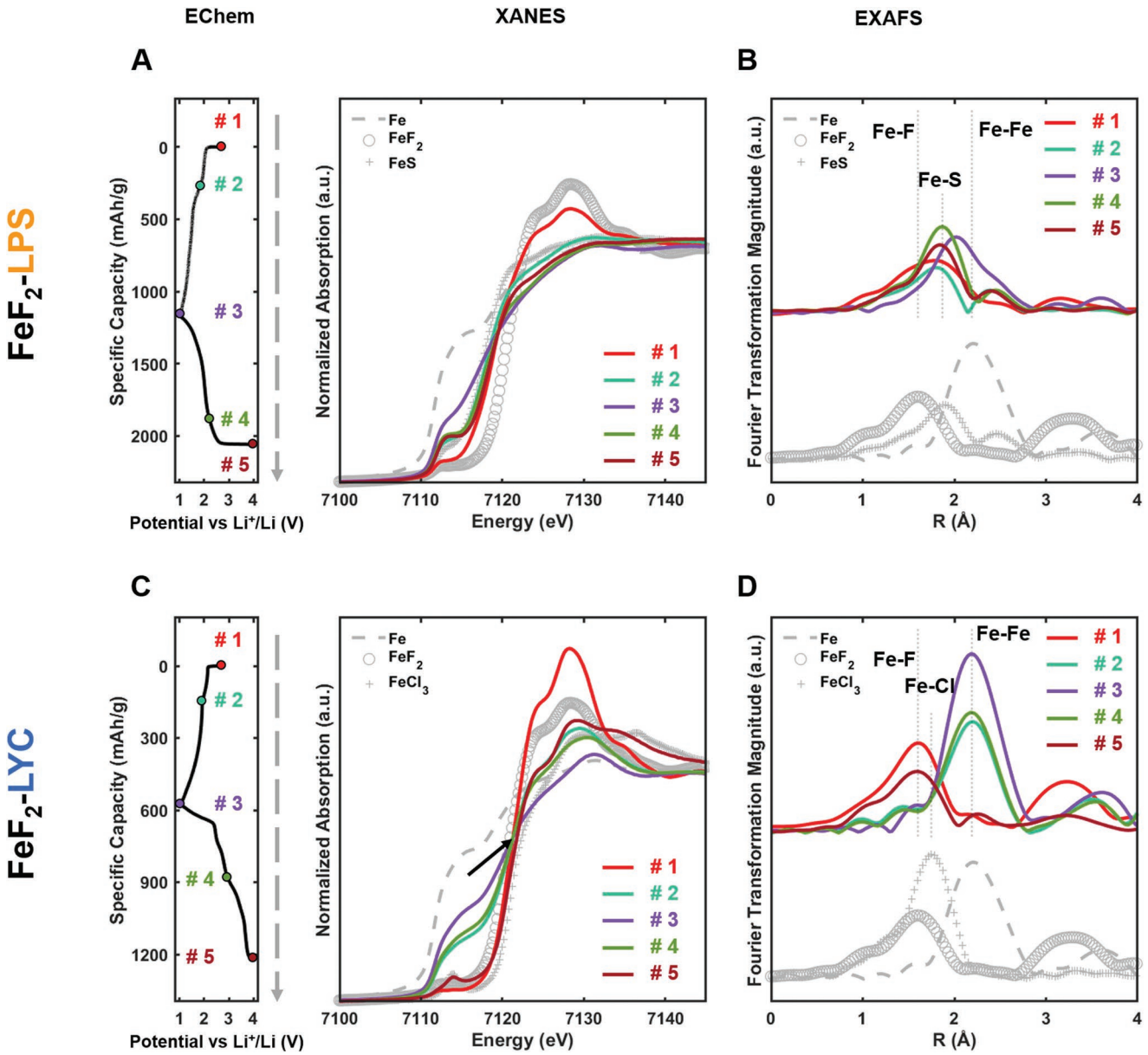

Figure 3. Ex situ XAS of Fe. Near-edge XAS spectra (XANES) for the Fe K-edge XAS results of A) FeF_2-LPS and C) FeF_2-LYC. Cutoff voltage has been labeled in the galvanostatic profiles with the corresponding colors. Fourier transformation of extended X-ray absorption fine structure (EXAFS) for the Fe K-edge of B) FeF_2-LPS and D) FeF_2-LYC.

energies, corresponding to the oxidization of Fe. Surprisingly, FeS, instead of FeF_2, seems to be the dominant phase in the fully charged sample (Figure 3B; Figure S8A, Supporting Information). A rough estimation from the LCA fitting result (Figure S6, Supporting Information) suggests that the relative molar fraction of FeS is >70% in the fully charged sample. The absence of FeS in the XRD results of the fully charged sample is probably due to the small size or low crystallinity. The reconversion of the FeF_2–LPS cathode to FeS during the charging process explains the low electrode potential as the theoretical potential of FeS is 1.76 V (Figure 2A).[52] Since the theoretical capacity of FeS (610 mA h g^{-1}) is much lower than the observed charging capacity, oxidization of P and S in the LPS are also involved in the redox process. The reduction and oxidization of P and S are further supported by XPS spectra of P 2p and S 2p after discharge and charge (Figure S9, Supporting Information). While we mainly studied the evolutions for the first charging process, the same reactions are also expected to occur during the subsequent charging process as the charge profile remains almost identical for the 2nd and 3rd cycle (Figure 2A).

During discharge of the FeF_2-LYC cathode, the absorption edge of XANES spectra shifts to low incident energy, ≈7110 eV, corresponding to the reduction of Fe. The increase of the characteristic Fe peak (Fe—Fe, first shell) and the decrease of the characteristic FeF_2 peak (Fe—F, first shell) in the EXAFS results (Figure 3D) suggest the formation of Fe through

© 2022 Wiley-VCH GmbH

electrochemical reduction. During charge, the XANES edge shifts back to higher incident energy as a result of oxidization. Interestingly, all the spectra except the fully charged one share a common point at ≈7121 eV. Such isosbestic point indicated by the arrow in Figure 3C suggests that reaction proceeds in a two-phase fashion up to 2.9 V. Correlating with the EXAFS results (Figure 3D), a gradual reconversion process from Fe to FeF_2 occurs during the initial charging process. Further charging to a high voltage (4 V at point 5) leads to oxidation of Fe^{2+} to Fe^{3+}. To identify the possible oxidization product at high voltages, we compared the XANES spectra of the fully charged electrode with the reference spectra of FeF_3 and $FeCl_3$ (Figure S8B, Supporting Information). It can be seen that the spectrum of the fully charged sample is similar to that of $FeCl_3$ near the rising edge, and therefore the high voltage plateau during the charging process is considered to correspond to the formation of $FeCl_3$-like compounds and this statement is also supported by the disappearance of LiCl in the XRD results at the end of charging process. Slight reduction and oxidization of LYC, or more specifically Y, might also occur during the charge and discharge process of FeF_2-LYC, as indicated by the XPS results (Figure S9, Supporting Information), but the contribution from the reversible electrolyte decomposition is much smaller than that in the FeF_2-LPS because of the superior anodic stability of halide-based electrolyte (Figure S3, Supporting Information).[42]

Based on the results from ex situ XRD and XAS, the possible reaction mechanisms of the cathodes are summarized. For FeF_2-LPS cathode, the two sloping plateaus at 2.1 and 1.9 V during the initial discharge are caused by the conversion of FeF_2 and FeS (formed during ball-mill synthesis of FeF_2-LPS), respectively. The reduction of LPS solid electrolyte also occurs during the first discharge process since the observed capacity is much higher than the theoretical capacity of FeF_2 and FeS. The sloping plateau at 2.1 V during the initial charging process can be attributed to the reconversion from Li_2S and Fe to FeS as well as the oxidation of P and S in the LPS, and these redox couples remain for the subsequent charge and discharge processes. For FeF_2-LYC cathode, the two sloping plateaus at 2.1 and 1.9 V during the initial discharging process can be attributed to the slight reduction of LYC and the conversion of FeF_2 to Fe and LiF, respectively. During charge, Fe and LiF will be reconverted back to FeF_2 and this process leads to the plateau at 2.4 V, and the high voltage plateau observed during the charging process at 3.4 V is caused by further oxidization of Fe^{2+} to $FeCl_3$. For the 2nd discharge process, $FeCl_3$ will first be reduced, followed by the conversion of FeF_2 to Fe and LiF, and a reverse process, i.e., the reconversion of FeF_2 and oxidization Fe^{2+} to $FeCl_3$, occurs during the subsequent charging.

2.3. Electrochemical Characterization of Crystalline and Amorphous FeF_2 Cathodes

We have thus far shown that the utilization of LYC SE can effectively improve the electrochemical reversibility as well as enable a complete conversion and reconversion of FeF_2 cathode during the charge and discharge processes. Even without sophisticated structural engineering, the FeF_2-LYC cathode composite consisting of crystalline FeF_2, glass–ceramic LYC, and carbon additive, already demonstrated a better cycling stability and lower voltage hysteresis (especially for the first cycle) than FeF_2 cathodes tested in liquid electrolytes (Figure S10, Supporting Information).[3,7,8,16,20,23,49,57–59] Since micron-sized regions that are rich in Fe and F are still observed in the cathode composites after 20 cycles (Figure S11, Supporting Information), further enhancing the performance is still possible by achieving a more uniform distribution of the components at nanoscale. We then tried to further improve the electrochemical performance of FeF_2-LYC, by amorphizating it through high-energy ball-milling, as amorphous transition metal sulfide cathodes have been reported to exhibit enhanced kinetics and cycling stability compared with the crystalline ones.[60–63] No apparent diffraction peaks, except for the sealing cover used to protect the sample during characterization, can be observed in the FeF_2-LYC cathode after high-energy ball-milling (**Figure 4**A), confirming the amorphous structure of the cathode. A uniform and nanoscale distribution of FeF_2, LYC, and carbon was achieved in the amorphous cathode based on the elemental mapping results (Figure S12, Supporting Information). Figure 4B,C compares the quasi-equilibrium potential of the crystalline and amorphous FeF_2-LYC cathode based on the galvanostatic intermittent titration technique (GITT) tests. The amorphous FeF_2-LYC cathode shows similar plateaus at low and high voltages as the crystalline cathode. Moreover, significant decreases in the overpotential at different SOCs can be observed for the amorphous cathode, confirming that amorphization of FeF_2-LYC can effectively improve the kinetics of the electrode. Figure 4D,E shows the Nyquist plots of the crystalline and amorphous electrodes respectively. Three frequencies (150 kHz, 100, and 10 Hz) were selected to show the evolution of resistances at different SOCs. The high-frequency semicircle (≈150 kHz) is attributed to the ionic resistance in the bulk and grain boundaries of the solid electrolyte. The semi-circle located at around the mid-frequency of ≈100 Hz is mainly attributed to the interfacial resistances. The tail appearing at a low frequency (≈10 Hz) corresponds to a Warburg region that can be assigned to the solid-state diffusion of Li ions inside the electrodes. Detailed fitting results of the Nyquist plots are shown in Figure S13 (Supporting Information), where a smaller increase in the interfacial resistance with SOC can be observed for the amorphous FeF_2-LYC cathode, consistent with the enhanced kinetics of amorphous electrodes.

Figure 5A,B compares the charge–discharge curves of the crystalline and amorphous FeF_2-LYC cathode. The amorphous cathode exhibits a lower overpotential than the crystalline one at each rate. The rate performance of the amorphous composite is higher than its crystalline counterpart, especially at a high rate (Figure 5C). At 1 C rate the amorphous FeF_2-LYC presents a capacity of 390 mA h g^{-1}, which is >50% higher than the capacity of the crystalline electrode tested at the same condition. Figure 5D compares the voltage hysteresis of the crystalline and amorphous FeF_2-LYC tested at a rate of 0.1 C at 60 °C. The result shows the amorphization of the FeF_2-LYC cathode can further reduce the voltage hysteresis to ≈0.45 V (at 50% SOC) at a rate of 0.1 C. Comparing the voltage hysteresis of FeF_2 with the literature value in a rigorous way is impossible due to the different testing conditions (e.g., current density, mass loading, temperature, etc.), but 0.45 V is among the lowest for FeF_2

© 2022 Wiley-VCH GmbH

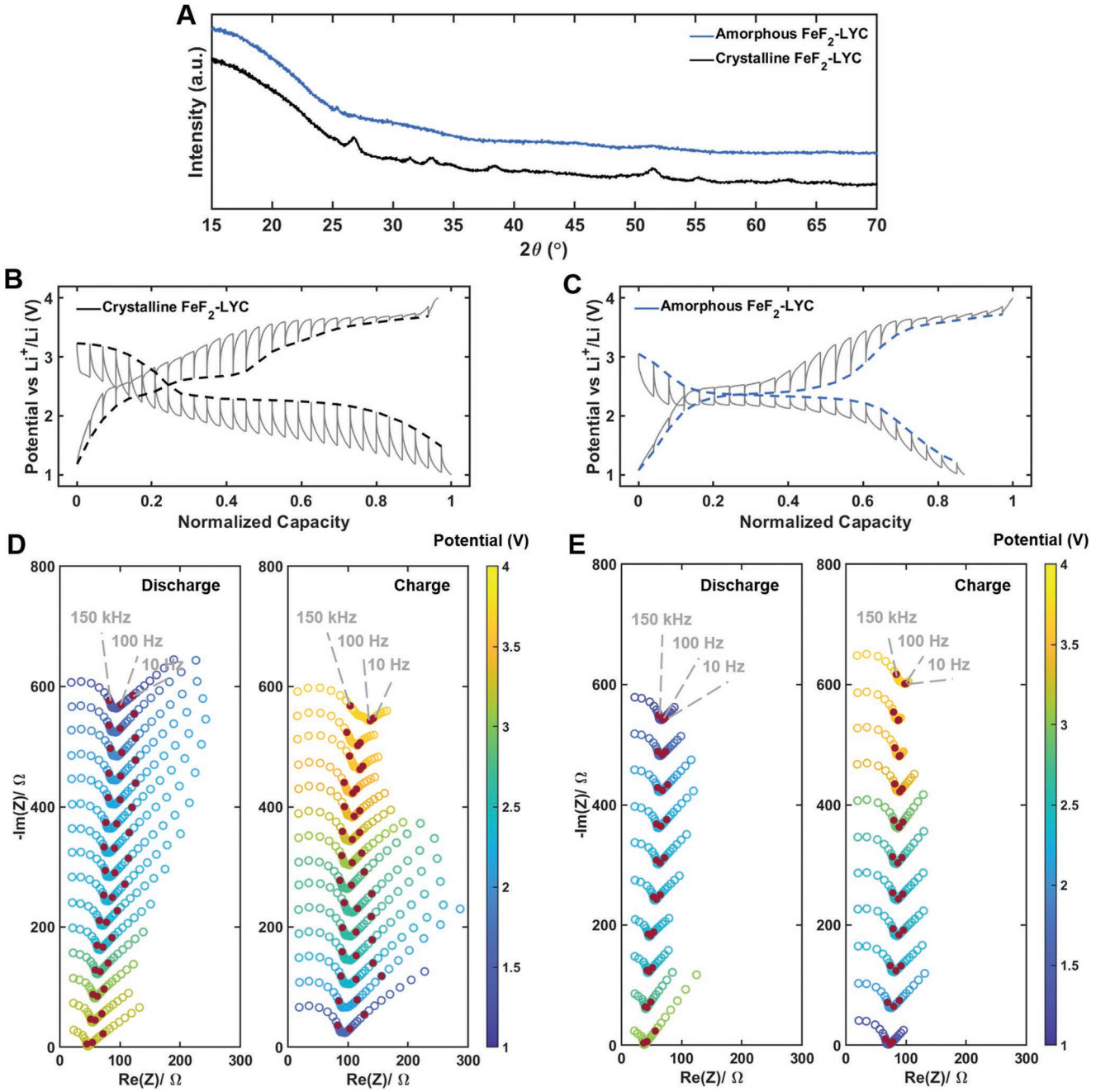

Figure 4. Quasi-equilibrium potential and impedance evolution of crystalline and amorphous FeF_2 cathode. A) Powder XRD pattern of amorphous and crystalline FeF_2-LYC composite. Broad rutile FeF_2 and glass-ceramic LYC peaks are apparent in the crystalline FeF_2-LYC composite. No diffraction peaks except the peak caused by the sealing cover are visible in the amorphous FeF_2-LYC composite. Quasi-equilibrium potential of FeF_2 cathode composite. Galvanostatic intermittent titration technique (GITT) measurement of B) crystalline FeF_2-LYC, and C) amorphous FeF_2-LYC. For the GITT measurement, the cells were charged/discharged at 0.1 C for 0.5 h followed by a 10 h rest. The grey solid lines indicate the voltage profile of the initial charge/discharge. The connected blue dash lines indicate the quasi-equilibrium potential at each normalized capacity. Impedance evolution of the D) crystalline FeF_2-LYC and E) amorphous FeF_2-LYC during discharge and charge. Each EIS pattern is measured after a 10 h rest at every state of charge.

cathode reported to date.[3,7,8,16,20,23,49,57–59] The quasi-equilibrium voltage hysteresis, i.e., the voltage hysteresis between the equilibrium potentials for charge and discharge using GITT, of amorphous FeF_2-LYC is comparable with or even smaller than that of the ternary metal fluorides and Co— and O— co-substituted iron fluorides (Figure S14, Supporting Information).[5,24] The excellent kinetics of the amorphous FeF_2-LYC cathode also enable its operation at room temperature with a decent performance (Figure S15, Supporting Information). The excellent rate performance of amorphous FeF_2-LYC cathode is also demonstrated by comparing with the previously reported iron fluoride cathodes tested at both room temperature and elevated

© 2022 Wiley-VCH GmbH

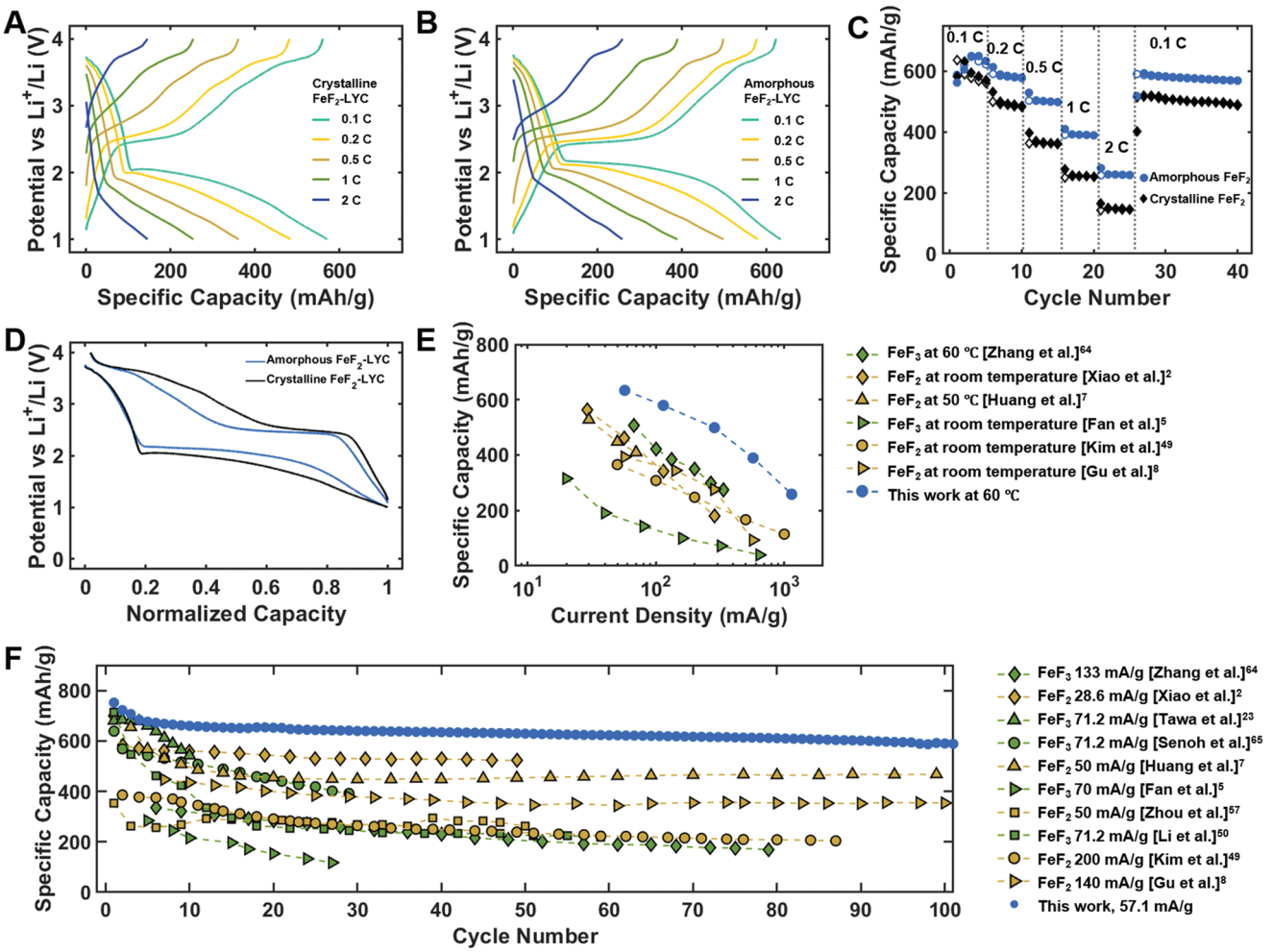

Figure 5. Electrochemical performance of crystalline and amorphous FeF_2-LYC cathode composite. Charge/discharge curves of A) crystalline FeF_2-LYC composite and B) amorphous FeF_2-LYC cathode at different current densities. C) Rate performance of the crystalline and amorphous FeF_2-LYC cathodes. D) Voltage hysteresis of the crystalline and amorphous FeF_2-LYC composite at a rate of 0.1 C. E) The discharge capacity of the amorphous FeF_2-LYC at different current densities and their comparison with previously reported iron fluoride cathodes.[2,5,7,8,49,64] F) Comparison of the cycling performance of amorphous FeF_2-LYC cathode with the data reported in the literature.[2,5,7,8,23,49,50,57,64,65] All the cells were tested at 60 °C unless specified.

temperatures (Figure 5E).[2,5,7,8,49,64] It should be noted that even a thick SE (≈1 mm) with a low ionic conductivity (≈10^{-4} S cm^{-1}) was used in this work, the rate performance of amorphous FeF_2-LYC at room temperature is still comparable with FeF_2 cathode tested in liquid electrolyte cells where a thin separator (tens of microns) is typically used with highly conductive liquid electrolyte (≈10^{-2} S cm^{-1}). The results indicates that amorphization of the FeF_2-LYC cathode composite can be used as an effective way to improve its kinetics. The exact mechanisms for the enhanced kinetics of the amorphous cathode need further study but it may be related to the more uniform, nanoscale distribution of FeF_2, LYC, and VGCF (Figure S12, Supporting Information) and the increase in the ionic conductivity of amorphous LYC.[60–63]

In addition to the excellent kinetic performance, the amorphous FeF_2-LYC cathode also exhibit great cycling performance, and the specific capacity is ≈600 mA h g^{-1} after 100 cycles when testing at 0.1 C at 60 °C after 100 cycles (Figure 5F). The coulombic efficiency of the FeF_2-LYC cathode kept at a value of higher than 99.7% during cycling (Figure S16, Supporting Information). The excellent cycling stability of amorphous FeF_2-LYC cathode also make it one of the most cycling stable iron fluoride cathodes reported to date (Figure 5F).[2,5,7,8,23,49,50,57,64,65] The superior cycling stability of the amorphous electrode was also demonstrated when testing it at 0.1 C at room temperature, minimal capacity decay can be observed when the cathode is cycled for 200 times (Figure S15, Supporting Information).

Our work highlights the important effect of SE on the redox behavior of iron fluoride. Irreversible transformation from FeF_2 to FeS occurs in a sulfide-based SE after the first discharge, while the utilization of chloride-based SE can enable a complete conversion and reconversion of FeF_2. The reaction mechanisms of FeF_2 with different SEs can be rationalized by the difference in the electrode potential of iron compounds. Based on a thermodynamic analysis,[52] the theoretical electrode potentials of iron fluorides (FeF_2: 2.63 V and FeF_3: 2.73 V) are higher than those of iron sulfides (FeS: 1.76 V and FeS_2: 1.87 V), but are comparable with or slightly lower than

© 2022 Wiley-VCH GmbH

iron chlorides ($FeCl_2$: 2.42 V and $FeCl_3$: 2.83 V). As has been discussed, the discharge process of FeF_2-LPS cathode involves the conversion of FeF_2 and FeS as well as the reduction of LPS, leading to the formation of Fe, LiF, Li_2S, and P-containing compounds with lower oxidization state of P at the end of discharge. During the charge of FeF_2-LPS cathode, the formation of iron sulfides is thermodynamically more favorable than that of iron fluorides. As long as there is sufficient Li_2S, which is likely the case in the FeF_2-LPS cathode based on the apparent decomposition of LPS, the reconversion from Fe and Li_2S to FeS will be the dominant reaction during charge. Based on this, iron fluoride cathodes can hardly exhibit their intrinsic redox behavior with sulfide-based SEs without significant coating. Although the FeF_2-LPS cathode delivers a higher capacity and stable cycling at a low rate (Figure S4, Supporting Information), its capacity is dominated by the redox reactions associated with SE and therefore these performances are heavily related to the SE (e.g., particle size, contacts with FeF_2 and carbon, intrinsic electronic conductivity) and are very difficult to control in practical applications. The consumption of too much SE in the cathode composite may also lead to kinetic issue due to the impeded transport of Li ions in the cathode composite. For FeF_2-LYC cathode, although slight reduction of LYC occurs with the conversion of FeF_2, the formation of $FeCl_2$ seems to be kinetically hindered. To our knowledge, the utilization of $FeCl_2$ as a conversion cathode for typical Li-ion batteries has not been reported. Therefore, a complete reconversion from Fe and LiF to FeF_2 can be achieved during the subsequent charging process. Further charging to a higher voltage of 4 V led to the formation of $FeCl_3$-like compound due to the higher electrode potential of $FeCl_3$ and insufficient LiF in the electrodes. More detailed insights about the reaction mechanisms of FeF_2 with different SEs may be provided by in situ characterizations[3] and/or computational study of the phase equilibria at different voltage of the cathode and SE composites.[18,66]

Although exceptional electrochemical performances of FeF_2 cathode can be achieved by the utilization of LYC SE, which validated the proposed hypothesis, the kinetic performance of solid-state FeF_2 cathode still needs to be improved. The voltage hysteresis of 0.45 V at a rate of 0.1 C at 60 °C is still too high for its practical application. As the voltage hysteresis of a conversion-type cathode is heavily related to the cathode active material itself, further lowering the voltage hysteresis is highly possible by integrating halide-based SE with cathode active materials that demonstrate low voltage hysteresis such as ternary metal fluorides[24] and Co— and O— substituted iron fluoride.[5] Further improvements in the ionic conductivity of halide-based SE and in the effective ionic conductivity of the cathode composite will also help improve the kinetics of the electrode.[46,67–70] The extremely small quasi-equilibrium voltage hysteresis observed from the GITT measurements (Figure S14, Supporting Information) supports the feasibility to further lowering the voltage hysteresis. It should be noted that solid-state batteries have its own challenges in maintaining the interfacial contact between solid electrode and SE over long-term charge/discharge cycles, especially for high-volume-change electrodes.[71,72] Nevertheless, this challenge may be mitigated by microstructure design, binder optimization and pressure control, as suggested by some recent works on cycling-stable silicon anodes in solid-state batteries.[73]

3. Conclusion

In summary, we report that the key challenges including electrochemical irreversibility, cycling instability, and sluggish kinetics of conversion-type iron fluoride cathodes could be addressed by utilizing SEs. Through detailed characterizations of the electrodes at various SOCs, we highlight the significant effect of SE compositions on the redox behavior of FeF_2 cathode, and halide-based LYC was demonstrated to enable a complete conversion and reconversion of FeF_2 that cannot be achieved with sulfide-based LPS SE. Due to restricted and reversible decomposition of LYC SE, prevention of transition metal dissolution, mechanical confinement of active materials, as well as improved kinetics, FeF_2 cathode demonstrated superior electrochemical performance in LYC SE compared with that in the conventional liquid electrolytes. Amorphization of the electrode was demonstrated to be an effective approach to further improve the performance of FeF_2–LYC cathode. We expect the same concept of utilizing halide-based SEs can be generalized to other conversion-type cathodes such as CuF_2. We hope our work could stimulate further research interest in the long-standing, low-cost, low-toxicity, and energy-dense conversion-type cathodes.

4. Experimental Section

Materials Synthesis: All chemicals were used as purchased without further purification. Lithium sulfide (Li_2S, 99.98%), phosphorous pentasulfide (P_4S_{10}, 99%), indium (99.99%), polytetrafluoroethylene (PTFE), and carbon nanofibers (VGCF) were purchased from Sigma–Aldrich. Lithium chloride (LiCl, 99.995%) and yttrium chloride (YCl_3, 99.9%) were purchased from Alfa Aesar. All handling of solids was performed in the Argon-filled glovebox to prevent exposure to moisture and oxygen.

Glass-ceramic LYC solid electrolyte was synthesized through high-energy ball milling.[42] The starting materials, LiCl and YCl_3, were mixed in the stoichiometric ratio and sealed in a ZrO_2 milling set. The mixture was ball-milled at 510 rpm for 50 h. The LPS glass was synthesized using the same ball-milling procedure but with different starting materials of Li_2S and P_4S_{10}. Li_6PS_5Cl electrolyte was prepared through solid state reaction method. The starting materials of Li_2S, P_4S_{10}, and LiCl were mixed in the stoichiometric ratio using a ZrO_2 milling set at 110 rpm for 6 h. The recovered powder was pelletized and sintered in a carbon-coated quartz ampoule at 550 °C for 24 h.

To prepare the cathode composite, FeF_2 were heated at 120 °C under vacuum overnight before sealed in a stainless-steel milling set. The powder was ball-milled at 300 rpm for 3 h with a ball to material ratio of sixty to reduce its particle size to nanometer scale. Nanosized FeF_2 powder was then mixed with carbon nanofiber by mechanical milling with VGCF in a stainless-steel milling set at 380 rpm for 10 h. The mixture of FeF_2 and VGCF was then mixed with solid electrolyte (LYC, LPS, or Li_6PS_5Cl) in the milling sets at 360 rpm for 1.5 h with a ball to material ratio of sixty. For all cathode composite, the weight ratio of FeF_2, VGCF, and solid electrolyte was 4:2:4. Amorphization of the FeF_2-LYC cathode composite was achieved by ball-milling the cathode composite with an increased ball to material ratio of 240. Hand-mixed samples were prepared by grounding the ball-milled FeF_2-VGCF nanocomposites with SEs using a mortar and pestle for 15 min. To prepare free-standing FeF_2

© 2022 Wiley-VCH GmbH

cathode composite film, 2 wt.% of PTFE was added into the as-prepared cathode composite powder through dry mixing using a mortar and pestle. The obtained mixture was rolled into a film at 80 °C.

Materials Characterization: A Carl Zeiss Supra 55 FESEM was used for the scanning electron microscopy and elemental mapping for the cathode composite. In order to investigate the structural evolution with cycling, cathode composites at different states of charge/discharge were prepared by setting various cutoff voltages in a galvanostatic cycling test at a rate of C/20. The all-solid-state electrodes were removed from the Swagelok cells in the glovebox. The cathode layers were sealed in the air-tight sample holder and transferred to XRD measurement. The XRD measurement was done on a PanAlytical X'Pert Diffractometer using a Cu Kα X-ray source from 15° to 70° 2θ, at a scan rate of 1.25 min^{-1}.

For XPS experiments, the fully charged/discharged samples were prepared by galvanostatic cycling at a rate of C/20. The electrodes were removed from the Swagelok cells and loaded on the XPS sample holders. The pristine, fully charged, or discharged samples were transferred on the holder with an air-tight transfer vial. The XPS characterization was performed with the PHI Versaprobe XPS system (Al K-alpha X-ray gun) at 53.6 W. Pass energy for survey (117.4 eV) and energy for detail spectra (23.5 eV). All spectra were charge-referenced to the disordered C 1s component at a binding energy of 284.8 eV. The XPS data were processed using the open-access software XPSPEAK41.

The samples for ex situ XAS measurement were prepared by setting different cutoff potentials in a galvanostatic cycling test at a rate of C/20. The all-solid-state electrodes were removed from the Swagelok cells and sealed in Kapton tapes in the glovebox. Reference spectra have been recorded including Fe, FeF_2, FeF_3, FeS, FeS_2, $FeCl_2$, and $FeCl_3$. The Fe K-edge XAS spectra were measured in fluorescence mode at 7-BM beamline (QAS) of National Synchrotron Light Source II (NSLS II), Brookhaven National Laboratory (BNL). The data was analyzed using the Athena software.[74]

The ex situ AES mapping samples were densified into pellets and the test was performed on the Auger Electron Spectroscope (Physical Electronics) at the Nanoscale Characterization Core of RPI.

Electrochemical Characterization: All-solid-state FeF_2 cells were assembled using a customized Swagelok cell. First, 80 mg of solid electrolyte was filled into a polyether ether ketone (PEEK) housing with an inner diameter of 10 mm and densified at a pressure of 100 MPa for 3 min. Cathode composite of 5 mg was then loaded at one side of the pellet and pressed at 350 MPa for 3 min. On the other side of the pellet, Li-In alloy anode was attached at 300 MPa for 1 min. Two stainless steel rods were applied as current collectors. To ensure the mechanical contact for the charge carrier percolation, a stack pressure of ≈60 MPa was applied using an external steel frame.

Galvanostatic cycling of the cell was carried out from 1.0 to 4.0 V versus Li/Li$^+$ at different rates using Arbin or LAND battery testing systems. The current densities for the rate performance test were calculated based on the theoretical capacity of FeF_2 (1 C = 571 mA h g^{-1}). GITT was performed by applying an intermittent current at 0.1 C for 30 min followed by a 10 h rest. The impedance at different states of charge was measured from 1.5 MHz to 1 Hz using a Gamry potentiostat.

Supporting Information

Supporting Information is available from the Wiley Online Library or from the author.

Acknowledgements

B.S., Y.H., and F.H. acknowledge the support from the US Department of Energy (DOE), Advanced Research Projects Agency for Energy (ARPA-E), IONICS program (Award No. DE-AR0000781). F.H. also acknowledges the support from the Priti and Mukesh Chatter Career Development Chair Professorship at the Rensselaer Polytechnic Institute. S.T., X.-Q.Y., and E.H. are supported by the Assistant Secretary for Energy Efficiency and Renewable Energy, Vehicle Technology Office of the US Department of Energy through the Advanced Battery Materials Research (BMR) Program under contract no. DE-SC0012704. This research used beamline 7-BM (QAS) of the National Synchrotron Light Source II, U.S. DOE Office of Science User Facilities, operated for the DOE Office of Science by Brookhaven National Laboratory under contract no. DE-SC0012704.

Conflict of Interest

The authors declare no conflict of interest.

Author Contributions

F.H. conceived the idea and supervised the project. B.S. prepared the materials, performed the electrochemistry tests, and conducted the ex situ XRD analysis. Y.H. assisted with the electrochemical tests. B.S. and S.T. prepared the samples for ex situ XAS characterization and performed the XAS tests. B.S. and L.Z. prepared the samples for ex situ XPS characterization and performed the XPS tests. B.S., S.T., E.H., and F.H. wrote the manuscript with the input from all the co-authors.

Data Availability Statement

The data that support the findings of this study are available from the corresponding author upon reasonable request.

Keywords

all-solid-state batteries, conversion-type iron fluoride cathodes, halide solid electrolytes, lithium-ion batteries

Received: June 15, 2022
Revised: September 14, 2022
Published online:

[1] V. Viswanathan, A. H. Epstein, Y.-M. Chiang, E. Takeuchi, M. Bradley, J. Langford, M. Winter, *Nature* **2022**, *601*, 519.
[2] A. W. Xiao, H. J. Lee, I. Capone, A. Robertson, T.-U. Wi, J. Fawdon, S. Wheeler, H.-W. Lee, N. Grobert, M. Pasta, *Nat. Mater.* **2020**, *19*, 644.
[3] X. Hua, A. S. Eggeman, E. Castillo-Martínez, R. Robert, H. S. Geddes, Z. Lu, C. J. Pickard, W. Meng, K. M. Wiaderek, N. Pereira, G. G. Amatucci, P. A. Midgley, K. W. Chapman, U. Steiner, A. L. Goodwin, C. P. Grey, *Nat. Mater.* **2021**, *20*, 841.
[4] J. Cabana, L. Monconduit, D. Larcher, M. R. Palacín, *Adv. Mater.* **2010**, *22*, E170.
[5] X. Fan, E. Hu, X. Ji, Y. Zhu, F. Han, S. Hwang, J. Liu, S. Bak, Z. Ma, T. Gao, S.-C. Liou, J. Bai, X.-Q. Yang, Y. Mo, K. Xu, D. Su, C. Wang, *Nat. Commun.* **2018**, *9*, 2324.
[6] K. Chen, M. Lei, Z. Yao, Y. Zheng, J. Hu, C. Lai, C. Li, *Sci. Adv.* **2021**, *7*, eabj1491.
[7] Q. Huang, K. Turcheniuk, X. Ren, A. Magasinski, A.-Y. Song, Y. Xiao, D. Kim, G. Yushin, *Nat. Mater.* **2019**, *18*, 1343.
[8] W. Gu, O. Borodin, B. Zdyrko, H.-T. Lin, H. Kim, N. Nitta, J. Huang, A. Magasinski, Z. Milicev, G. Berdichevsky, G. Yushin, *Adv. Funct. Mater.* **2016**, *26*, 1507.
[9] H. Wan, L. Cai, F. Han, J. P. Mwizerwa, C. Wang, X. Yao, *Small* **2019**, *15*, 1905849.

 © 2022 Wiley-VCH GmbH

[10] T. A. Yersak, H. A. Macpherson, S. C. Kim, V.-D. Le, C. S. Kang, S.-B. Son, Y.-H. Kim, J. E. Trevey, K. H. Oh, C. Stoldt, S.-H. Lee, *Adv. Energy Mater.* **2013**, *3*, 120.
[11] G. F. Dewald, Z. Liaqat, M. A. Lange, W. Tremel, W. G. Zeier, *Angew. Chem., Int. Ed.* **2021**, *60*, 17952.
[12] H. Pan, M. Zhang, Z. Cheng, H. Jiang, J. Yang, P. Wang, P. He, H. Zhou, *Sci. Adv.* **2022**, *8*, eabn4372.
[13] Y. Liu, X. Meng, Z. Wang, J. Qiu, *Sci. Adv.* **2022**, *8*, eabl8390.
[14] M. Shaibani, M. S. Mirshekarloo, R. Singh, C. D. Easton, M. C. D. Cooray, N. Eshraghi, T. Abendroth, S. Dörfler, H. Althues, S. Kaskel, A. F. Hollenkamp, M. R. Hill, M. Majumder, *Sci. Adv.* **2020**, *6*, eaay2757.
[15] P. Poizot, S. Laruelle, S. Grugeon, L. Dupont, J.-M. Tarascon, *Nature* **2000**, *407*, 496.
[16] F. Badway, F. Cosandey, N. Pereira, G. G. Amatucci, *J. Electrochem. Soc.* **2003**, *150*, A1318.
[17] H. Li, P. Balaya, J. Maier, *J. Electrochem. Soc.* **2004**, *151*, A1878.
[18] R. E. Doe, K. A. Persson, Y. S. Meng, G. Ceder, *Chem. Mater.* **2008**, *20*, 5274.
[19] N. Yamakawa, M. Jiang, B. Key, C. P. Grey, *J. Am. Chem. Soc.* **2009**, *131*, 10525.
[20] F. Wang, R. Robert, N. A. Chernova, N. Pereira, F. Omenya, F. Badway, X. Hua, M. Ruotolo, R. Zhang, L. Wu, V. Volkov, D. Su, B. Key, M. S. Whittingham, C. P. Grey, G. G. Amatucci, Y. Zhu, J. Graetz, *J. Am. Chem. Soc.* **2011**, *133*, 18828.
[21] F. Wang, H.-C. Yu, M.-H. Chen, L. Wu, N. Pereira, K. Thornton, A. Van der Ven, Y. Zhu, G. G. Amatucci, J. Graetz, *Nat. Commun.* **2012**, *3*, 1201.
[22] K. Karki, L. Wu, Y. Ma, M. J. Armstrong, J. D. Holmes, S. H. Garofalini, Y. Zhu, E. A. Stach, F. Wang, *J. Am. Chem. Soc.* **2018**, *140*, 17915.
[23] S. Tawa, K. Matsumoto, R. Hagiwara, *J. Electrochem. Soc.* **2019**, *166*, A2105.
[24] F. Wang, S.-W. Kim, D.-H. Seo, K. Kang, L. Wang, D. Su, J. J. Vajo, J. Wang, J. Graetz, *Nat. Commun.* **2015**, *6*, 6668.
[25] P. G. Bruce, L. J. Hardwick, K. M. Abraham, *MRS Bull.* **2011**, *36*, 506.
[26] Y. Sun, H.-W. Lee, G. Zheng, Z. W. Seh, J. Sun, Y. Li, Y. Cui, *Nano Lett.* **2016**, *16*, 1497.
[27] L. F. Olbrich, A. W. Xiao, M. Pasta, *Curr. Opin. Electrochem.* **2021**, *30*, 100779.
[28] P. Liu, J. J. Vajo, J. S. Wang, W. Li, J. Liu, *J. Phys. Chem. C* **2012**, *116*, 6467.
[29] L. Li, R. Jacobs, P. Gao, L. Gan, F. Wang, D. Morgan, S. Jin, *J. Am. Chem. Soc.* **2016**, *138*, 2838.
[30] F. Han, Y. Zhu, X. He, Y. Mo, C. Wang, *Adv. Energy Mater.* **2016**, *6*, 1501590.
[31] J. Janek, W. G. Zeier, *Nat. Energy* **2016**, *1*, 16141.
[32] X. Fan, X. Ji, F. Han, J. Yue, J. Chen, L. Chen, T. Deng, J. Jiang, C. Wang, *Sci. Adv.* **2018**, *4*, eaau9245.
[33] A. C. Luntz, J. Voss, K. Reuter, *J. Phys. Chem. Lett.* **2015**, *6*, 4599.
[34] J. M. Whiteley, S. Hafner, S. S. Han, S. C. Kim, K. H. Oh, S.-H. Lee, *Adv. Energy Mater.* **2016**, *6*, 1600495.
[35] F. Han, T. Gao, Y. Zhu, K. J. Gaskell, C. Wang, *Adv. Mater.* **2015**, *27*, 3473.
[36] Y. Kato, S. Hori, T. Saito, K. Suzuki, M. Hirayama, A. Mitsui, M. Yonemura, H. Iba, R. Kanno, *Nat. Energy* **2016**, *1*, 16030.
[37] N. Kamaya, K. Homma, Y. Yamakawa, M. Hirayama, R. Kanno, M. Yonemura, T. Kamiyama, Y. Kato, S. Hama, K. Kawamoto, A. Mitsui, *Nat. Mater.* **2011**, *10*, 682.
[38] F. Omenya, N. J. Zagarella, J. Rana, H. Zhang, C. Siu, H. Zhou, B. Wen, N. A. Chernova, L. F. J. Piper, G. Zhou, M. S. Whittingham, *ACS Appl. Energy Mater.* **2019**, *2*, 5243.
[39] X. Wang, W. Gu, J. T. Lee, N. Nitta, J. Benson, A. Magasinski, M. W. Schauer, G. Yushin, *Small* **2015**, *11*, 5164.
[40] F. Wu, V. Srot, S. Chen, M. Zhang, P. A. van Aken, Y. Wang, J. Maier, Y. Yu, *ACS Nano.* **2021**, *15*, 1509.
[41] A. Hayashi, S. Hama, H. Morimoto, M. Tatsumisago, T. Minami, *J. Am. Ceram. Soc.* **2001**, *84*, 477.
[42] T. Asano, A. Sakai, S. Ouchi, M. Sakaida, A. Miyazaki, S. Hasegawa, *Adv. Mater.* **2018**, *30*, 1803075.
[43] X. Li, J. Liang, K. R. Adair, J. Li, W. Li, F. Zhao, Y. Hu, T.-K. Sham, L. Zhang, S. Zhao, S. Lu, H. Huang, R. Li, N. Chen, X. Sun, *Nano Lett.* **2020**, *20*, 4384.
[44] Y. Liu, S. Wang, A. M. Nolan, C. Ling, Y. Mo, *Adv. Energy Mater.* **2020**, *10*, 2002356.
[45] C. Wang, J. Liang, J. Luo, J. Liu, X. Li, F. Zhao, R. Li, H. Huang, S. Zhao, L. Zhang, J. Wang, X. Sun, *Sci. Adv.* **2021**, *7*, eabh1896.
[46] L. Zhou, T.-T. Zuo, C. Y. Kwok, S. Y. Kim, A. Assoud, Q. Zhang, J. Janek, L. F. Nazar, *Nat. Energy* **2022**, *7*, 183.
[47] J. Liang, X. Li, K. R. Adair, X. Sun, *Acc. Chem. Res.* **2021**, *54*, 1023.
[48] B. Zahiri, A. Patra, C. Kiggins, A. X. B. Yong, E. Ertekin, J. B. Cook, P. V. Braun, *Nat. Mater.* **2021**, *10*, 1392.
[49] S. Kim, J. Liu, K. Sun, J. Wang, S. J. Dillon, P. V. Braun, *Adv. Funct. Mater.* **2017**, *27*, 1702783.
[50] C. Li, X. Mu, P. A. van Aken, J. Maier, *Adv. Energy Mater.* **2013**, *3*, 113.
[51] R. Koerver, F. Walther, I. Aygün, J. Sann, C. Dietrich, W. G. Zeier, J. Janek, *J. Mater. Chem. A* **2017**, *5*, 22750.
[52] C.-X. Zu, H. Li, *Energy Environ. Sci.* **2011**, *4*, 2614.
[53] W. M. Dose, C. S. Johnson, *Curr. Opin. Electrochem.* **2022**, *31*, 100827.
[54] Y. Sun, H.-W. Lee, Z. W. Seh, N. Liu, J. Sun, Y. Li, Y. Cui, *Nat. Mater.* **2016**, *1*, 15008.
[55] K. Tirez, G. Silversmit, L. Vincze, K. Servaes, C. Vanhoof, M. Mertens, N. Bleux, P. Berghmans, *J. Anal. At. Spectrom.* **2011**, *26*, 517.
[56] B. Ajiboye, O. O. Akinremi, A. Jürgensen, *Soil Sci. Soc. Am. J.* **2007**, *71*, 1288.
[57] J. Zhou, D. Zhang, X. Zhang, H. Song, X. Chen, *ACS Appl. Mater. Interfaces* **2014**, *6*, 21223.
[58] F. Cosandey, J. F. Al-Sharab, F. Badway, G. G. Amatucci, P. Stadelmann, *Microsc. Microanal.* **2007**, *13*, 87.
[59] F. Badway, N. Pereira, F. Cosandey, G. G. Amatucci, *J. Electrochem. Soc.* **2003**, *150*, A1209.
[60] T. Matsuyama, A. Hayashi, T. Ozaki, S. Mori, M. Tatsumisago, *J. Mater. Chem. A* **2015**, *3*, 14142.
[61] T. Matsuyama, A. Hayashi, C. J. Hart, L. F. Nazar, M. Tatsumisago, *J. Electrochem. Soc.* **2016**, *163*, A1730.
[62] X. Wang, K. Du, C. Wang, L. Ma, B. Zhao, J. Yang, M. Li, X.-X. Zhang, M. Xue, J. Chen, *ACS Appl. Mater. Interfaces* **2017**, *9*, 38606.
[63] H. Ye, L. Wang, S. Deng, X. Zeng, K. Nie, P. N. Duchesne, B. Wang, S. Liu, J. Zhou, F. Zhao, N. Han, P. Zhang, J. Zhong, X. Sun, Y. Li, Y. Li, J. Lu, *Adv. Energy Mater.* **2017**, *7*, 1601602.
[64] Y. Zhang, J. Meng, K. Chen, H. Wu, J. Hu, C. Li, *ACS Energy Lett.* **2020**, *5*, 1167.
[65] H. Senoh, K. Matsui, M. Shikano, T. Okumura, H. Kiuchi, K. Shimoda, K. Yamanaka, T. Ohta, T. Fukunaga, H. Sakaebe, E. Matsubara, *ACS Appl. Mater. Interfaces* **2019**, *11*, 30959.
[66] W. D. Richards, L. J. Miara, Y. Wang, J. C. Kim, G. Ceder, *Chem. Mater.* **2016**, *28*, 266.
[67] P. Minnmann, L. Quillman, S. Burkhardt, F. H. Richter, J. Janek, *J. Electrochem. Soc.* **2021**, *168*, 040537.
[68] A. Bielefeld, D. A. Weber, R. Rueß, V. Glavas, J. Janek, *J. Electrochem. Soc.* **2022**, *169*, 020539.
[69] H. Kwak, S. Wang, J. Park, Y. Liu, K. T. Kim, Y. Choi, Y. Mo, Y. S. Jung, *ACS Energy Lett.* **2022**, 1776.

© 2022 Wiley-VCH GmbH

[70] A. L. Davis, V. Goel, D. W. Liao, M. N. Main, E. Kazyak, J. Lee, K. Thornton, N. P. Dasgupta, *ACS Energy Lett.* **2021**, *6*, 2993.
[71] Y. Huang, B. Shao, F. Han, *Curr. Opin. Electrochem.* **2022**, *33*, 100933.
[72] J. M. Larson, E. Gillette, K. Burson, Y. Wang, S. B. Lee, J. E. Reutt-Robey, *Sci. Adv.* **2018**, *4*, eaas8927.
[73] D. H. S. Tan, Y.-T. Chen, H. Yang, W. Bao, B. Sreenarayanan, J.-M. Doux, W. Li, B. Lu, S.-Y. Ham, B. Sayahpour, J. Scharf, E. A. Wu, G. Deysher, H. E. Han, H. J. Hah, H. Jeong, J. B. Lee, Z. Chen, Y. S. Meng, *Science* **2021**, *373*, 1494.
[74] B. Ravel, M. Newville, *J. Synchrotron Radiat.* **2005**, *12*, 537.

© 2022 Wiley-VCH GmbH